Mon. Not. R. Astron. Soc. **000**, 1–15 (2016) Printed 6 January 2017 (MN LATEX style file v2.2)

Phase-space structure analysis of self-gravitating collisionless spherical systems

A. Halle[1,2⋆], S. Colombi[1] and S. Peirani[1]
[1] *UPMC-CNRS, UMR7095, Institut d'Astrophysique de Paris, 98 bis boulevard Arago, 75014 Paris, France*
[2] *Max Planck Institut für Astrophysik, Karl-Schwarzschild-Strasse 1, D-85741 Garching bei München, Germany*

arXiv:1701.01384v1 [astro-ph.GA] 5 Jan 2017

6 January 2017

ABSTRACT

We study the detailed phase-space structure of collisionless self-gravitating spherical systems with initial power-law density profiles $\rho(r) \propto r^n$, n ranging from 0 to -1.5, and Gaussian velocity dispersions. Two sub-classes of models are considered, with initial virial ratios $\eta = 0.5$ ("warm") and $\eta = 0.1$ ("cold"). To perform the analyses and control all sources of numerical artefacts, we use three kinds of codes: a Vlasov and a shell code preserving spherical symmetry, and the public N-body treecode `Gadget-2`. In all the simulations, the system first experiences a quiescent mixing phase during which it displays, in phase-space, a smooth spiral structure whose properties agree well with predictions from self-similar collapse when either inertial or gravitational force dominates. At some point, all the simulations display some level of radial instability, particularly in the cold case, where some macroscopic resonant modes destroy the spiral, but preserve the coarse-grained structure of the system, particularly the projected density profile $\rho(r)$, except for the `Gadget-2` simulations with $n \lesssim -1$. The latter are subject to radial orbit instability and thus have a slightly less contrasted central density profile than Vlasov or shells simulations. Yet, the early, quiescent evolution dominated by a folding spiral are quite representative of the system at later time at the coarse-grained level. The non-random nature of this spiral probably prevents the success of entropy maximisation in finding the quasi-stationary state. However, the good agreement with self-similar predictions might be promising for the study of the fine-grained structure of such systems.

Key words: gravitation – methods: numerical – galaxies: kinematics and dynamics – dark matter.

1 INTRODUCTION

Dark matter in the Universe and stars in galaxies behave like a self-gravitating collisionless fluid of which the dynamics can be described by the Vlasov-Poisson system :

$$\frac{\partial f}{\partial t} + \mathbf{v} \cdot \frac{\partial f}{\partial \mathbf{x}} - \frac{\partial \phi}{\partial \mathbf{x}} \cdot \frac{\partial f}{\partial \mathbf{v}} = 0, \tag{1}$$

$$\triangle \, \phi = 4\pi G \rho = 4\pi G \int f(\mathbf{x}, \mathbf{v}, t) \mathrm{d}\mathbf{v}, \tag{2}$$

where $f(\mathbf{x}, \mathbf{v}, t)$ is the phase-space density of the fluid at position $\mathbf{x}$, velocity $\mathbf{v}$ and time t, ρ is the mass density and ϕ is the gravitational potential.

A major issue when considering the dynamics of dark matter halos, elliptical galaxies and star clusters in the non collisional regime is to understand the establishment of quasi-stationary states that build up after a number of dynamical times, e.g. the famous NFW profile for dark matter halos (Navarro, Frenk, & White 1996, 1997). One way to relate initial to quasi-equilibrium state is to assume that the system reaches maximum entropy state after *violent relaxation* phase with strong mixing (Lynden-Bell 1967). However, when tested against numerical experiments, the maximum entropy approach is at best partly successful (see, e.g. Arad & Johansson 2005; Yamaguchi 2008; Joyce & Worrakitpoonpon 2011, and references therein) and the only way to improve the results is to introduce additional constraints and ad hoc ingredients (see, e.g. Hjorth & Williams 2010; Pontzen & Governato 2013; Carron & Szapudi 2013). Indeed, relaxation might be incomplete, that is not sufficiently random for the system to approach maximum entropy state. Detailed numerical study of the fine structure in phase-space structure of self-gravitating systems seems thus essential to understand mixing processes during the violent relaxation phase.

Another popular alternative to try understanding the

⋆ E-mail: halle@iap.fr (AH)

establishment of quasi-stationary profiles consists in investigating the subspace of self-similar solutions (see, e.g., Fillmore & Goldreich 1984; Bertschinger 1985; Henriksen & Widrow 1995; Sikivie et al. 1997; Mohayaee & Shandarin 2006; Alard 2013, but this list is far from exhaustive). While it is difficult to actually demonstrate the onset of self-similarity, it seems to be a natural outcome of gravitational dynamics. Self-similar solutions have been mostly derived in the cold case, i.e. in the case the phase-space distribution function is of zero initial velocity dispersion and can thus be viewed as a D-dimensional phase-space sheet moving in $2D$ phase-space. Self-similarity can apply as well to the warm case, but one expects it to take place only in a finite dynamical range due to the thickness of the phase-space sheet induced by the finite initial velocity dispersion. Although self-similarity is certainly compatible with a random relaxation process, in the current calculations performed in the literature, it is generally obtained through a perfectly deterministic process during which a regular spiral pattern is built up in phase-space.

The above approaches, along with perturbation theory in cosmological systems (see, e.g. Bernardeau et al. 2002), provide some partial analytical framework to study the Vlasov-Poisson system. However, in general, these equations usually require a numerical approach, which consists in decomposing the phase-space distribution function on an ensemble of macro-particles interacting with each other with a softened gravitational force (see, e.g. Hockney & Eastwood 1988; Bertschinger 1998; Colombi 2001; Dolag et al. 2008; Dehnen & Read 2011, for reviews on the subject). An alternative way, easily tractable in a small number of dimensions or for systems with a high level of symmetry, consists in using direct Vlasov solvers where the phase-space distribution function is generally sampled on an Eulerian mesh (see, e.g. Cheng & Knorr 1976; Fujiwara 1983; Filbet, Sonnendrücker, & Bertrand 2001; Besse & Sonnendrücker 2003; Alard & Colombi 2005; Colombi et al. 2015, and references therein), but there are many other approaches (see the extensive review in the introduction of Sousbie & Colombi 2016). Even though its remains numerically challenging in a high number of dimensions, the direct approach is becoming tractable thanks to the ever-increasing power of supercomputers (Yoshikawa et al. 2013).

In all the cases, validating the results obtained from numerical resolution of Vlasov-Poisson equations remains difficult. In particular, N-body results are often the object of debates. For instance, the close N-body encounters and collective effects due to particle shot noise can have some dramatic, possibly cumulative effects (see, e.g. Aarseth, Lin, & Papaloizou 1988; Kandrup & Smith 1991; Boily, Athanassoula, & Kroupa 2002; Binney 2004; Joyce, Marcos, & Sylos Labini 2009; Colombi et al. 2015), particularly when initial conditions are cold or close to cold (see, e.g., Melott et al. 1997; Melott 2007). While Vlasov codes do not use particles, they are still subject to non trivial numerical effects, because a phase-space grid still remains a discrete representation of the system (see, e.g. Colombi et al. 2015, hereafter C15). But since the numerical implementation is still different from N-body codes, a comparison between Vlasov and N-body codes seems appropriate and timely, especially when trying to analyse in detail the quasi-stationary state reached in the fluid limit by astrophysical systems.

One question indeed remains open. Are the quasi-stationary states obtained in the fluid limit for astrophysical systems mainly the result of a random process or a mere deterministic one, like for instance the spiral structure obtained in self-similar solutions? We propose here to approach this question by studying the evolution of a number of initially spherical systems with various initial density profiles and velocity dispersions. Spherical symmetry will allow us to compare high resolution Vlasov simulations to N-body simulations. Our analyses will focus on the detailed structure of the phase-space distribution function and comparisons with predictions from self-similarity.

More specifically, assuming $G = 1$ and following the footsteps of Hozumi, Fujiwara, & Kan-Ya (1996), we perform a number of controlled numerical experiments of unity total mass systems, initially spherical with a power-law density profile and a Gaussian isotropic velocity dispersion:

$$f(\mathbf{r},\mathbf{v}) = \frac{\rho_0(r)}{(2\pi\sigma_r^2)^{3/2}}\exp\left(-\frac{1}{2}\frac{v^2}{\sigma_r^2}\right), \quad r \leqslant R_0, \quad (3)$$

$$\rho_0(r) \propto r^n, \quad (4)$$

with $R_0 = 2$ the initial radius of the sphere and the initial slope spanning the range $n = 0$ to $n = -1.5$. We consider "warm" and "cold" cases defined by their respective value of the virial ratio, $\eta = 0.5$ and 0.1, with

$$\eta \equiv \frac{2T}{|W|}, \quad (5)$$

where T is the total kinetic energy and W the total potential energy of the system.

In these simulations, we aim to study in detail the evolution of the phase-space distribution function, the onset of instabilities and the consequence of these at the coarse-grained level. We shall also relate our measurements of fine details of the spiral pattern of the phase-space distribution to expectations from self-similar dynamics (see, e.g. Alard 2013, hereafter A13). To perform our simulations, we use three kinds of codes: a spherical semi-Lagrangian Vlasov solver, `VlaSolve`, presented in C15, the N-body public treecode `Gadget-2` (Springel 2005) and a standard spherical shells N-body code (see, e.g. Hénon 1964). Importantly enough, while the systems are forced to remain spherical in `VlaSolve` and in the shell code, it is not the case for `Gadget-2`. In particular, we shall see, as well known in the literature (see, e.g. Cannizzo & Hollister 1992; Hozumi, Fujiwara, & Kan-Ya 1996), that in the cold case, initially steep density profiles ($n = -1$ and $n = -1.5$) are subject to radial orbit instability triggered by the noise due to the discrete nature of the particle distribution. Importantly, the various codes employed in this work will allow us to understand in detail the nature of different sources of instabilities, in particular to disentangle true physical instabilities from numerical ones. The main goal of this numerical investigation is to justify the fact that being able to build an analytical theory for the dynamics of the spiral appearing in the early stages of the history of the system might be enough to capture the main aspect of its dynamics, be it even subject to subsequent instabilities that destroy the spiral structure.

This paper is organized as follows. In § 2, we present the numerical codes used to perform the simulations and provide details on the various runs we performed. In § 3, we perform a detailed visual inspection of the phase-space dis-

tribution function and discuss its projected density profile. Then, section 4 deals with self-similarity: we show how the calculations of A13 can be extended to spherical systems in a very simple way, and compare theoretical predictions to our numerical experiments. Finally, § 5 summarizes and discusses the results.

2 THE SIMULATIONS

In spherical symmetry, Vlasov equation can be written as:

$$\frac{\partial f}{\partial t} + v_r \frac{\partial f}{\partial r} + \left(\frac{j^2}{r^3} - \frac{GM(<r)}{r^2} \right) \frac{\partial f}{\partial v_r} = 0, \qquad (6)$$

with r the spherical radius, v_r the radial velocity and j the conserved angular momentum as coordinates and $M(<r)$ is the mass contained in a sphere of radius r. For a given value j of the angular momentum, the evolution is thus driven by the interplay between gravitational force, dominating at large radii, and centrifugal force j^2/r^3, dominating at small radii.

To solve equation (6), we have resorted to two numerical methods.

Firstly and mainly, we employ the spherical Vlasov solver `VlaSolve` presented in C15. This semi-Lagrangian code is similar to that of Fujiwara (1983) and thus uses the splitting algorithm of Cheng & Knorr (1976) to compute the evolution of the phase-space density on a mesh. The phase-space is divided into three-dimensional cells along radius, radial velocity, and angular momentum. A logarithmic scaling is used for radius to properly resolve the dynamics of the collapse at low radii, making the use of a minimum radius $R_{\rm min}$ necessary. To compute accurately the dynamics at low radii, the exact time spent by matter elements inside the sphere of radius $R_{\rm min}$ is computed assuming that gravitational force is negligible, which is an improvement over previous implementations which used the reflecting sphere method (see, e.g. Gott & Thuan 1976; Fujiwara 1983). More algorithmic details and tests of the code can be found in C15. Unless specified later, the grid for all the simulations is such that $(N_r, N_v, N_j) = (2048, 2048, 128)$, where N_r is the number of vertices of radius in log scale, N_v is the number of vertices of radial velocity in linear scale, and N_j is the number of slices of angular momentum such that the $k^{\rm th}$ slice contains fluid of angular momentum $j_{\rm max}\left((k-1/2)/N_j\right)^2$, corresponding formally to the interval $[j_{\rm max}\left((k-1)/N_j\right)^2, j_{\rm max}\left(k/N_j\right)^2]$. The computation domain is $\log_{10} R_{\rm min} \equiv -2 < \log_{10}(r) < 1.4$, $-v_l < v_r < v_l$ and $0 < j < 1.6$, where $v_l = 2$ for the runs with a virial ratio $\eta = 0.5$ and $v_l = 3$ for the runs with a virial ratio $\eta = 0.1$. The limits are chosen such that almost all the mass of the system is contained in the computing domain during the simulated time, except for matter elements passing inside the sphere of radius $R_{\rm min}$ or those escaping from the system at large radius. For all the simulations, the time step was chosen to be constant, equal to $\Delta t = 0.005$, a value larger than in C15 to avoid excessive diffusion due to over-frequent re-samplings of the phase-space distribution function, but we checked it is still on the safe side.

To avoid excessive aliasing effects in the `VlaSolve` runs, we apodize the initial profile given by equation (4) as follows,

$$f(\mathbf{r},\mathbf{v}) = \frac{\rho_0(r)}{(2\pi\sigma_r^2)^{3/2}} \exp\left(-\frac{1}{2}\frac{v^2}{\sigma_r^2}\right) \times \frac{1}{2}\left[1 + \mathrm{erf}\left(\frac{R_0 - r}{\Delta}\right)\right], \quad r \leqslant R_0, \qquad (7)$$

with $\Delta = 1/2$, exactly as in C15. This apodization slightly changes the value of the virial ratio, of the order of 10 percent at most.

The second code we use relies on the standard spherical shells approach as in e.g. Hénon (1964) and Gott & Thuan (1976). Note that we employ it only for the most critical cases, namely $(\eta, n) = (0.1, -1)$ and $(\eta, n) = (0.1, -1.5)$, when the results from `Gadget-2` differ too much from `VlaSolve`. In this N-body code, each particle represents a shell in configuration space and interacts with the other particles through gravitational force, $-GM(<r)/r^2$, which can be obtained very easily with a sorting procedure. The resolution of the Lagrangian equations of motion of the particles is performed simply with a leapfrog integrator with a constant time step $dt = 0.001$, five times smaller than the one chosen for the Vlasov code. Similarly as in `Vlasolve`, the Leapfrog algorithm is implemented using a decomposition of the Hamiltonian of the motion into a fully analytical drift part including inertial force and a kick part including solely gravitational force (see, e.g. Colombi & Touma 2008). Initial shells distribution consists simply in taking the initial conditions of the `Gadget-2` simulations described below, with the radius of each shell being equal to the magnitude of the position of each particle and their respective radial velocities and angular momenta directly derived from the three coordinates of the particle velocities.

Finally, we perform simulations using the public three-dimensional N-body treecode `Gadget-2` (Springel 2005) in its non cosmological set-up and with the treecode part only. The positions and velocities of particles are generated in a random way using a standard rejection method. Firstly, a random radius is generated directly according to the statistical law imposed by the density profile. The three dimensional coordinates of the particles are then set by computing a random direction isotropically distributed on the sphere. Secondly, a random Gaussian velocity is generated by standard rejection using the fact that the probability that a particle of given random velocity coordinates in the finite (hence truncated) domain $[-v_{\rm max}, v_{\rm max}]$ is kept is proportional to $\exp[-v^2/(2\sigma_r^2)]$, with $v_{\rm max} = 2$. Finally, a final rejection procedure is used to give account of the additional apodization of the density profile in equation (7).

In the `Gadget-2` simulations, spherical symmetry is no longer imposed, which leaves room for the development of angular anisotropies due to Poisson fluctuations in the initial particle distribution, even though the profile is initially spherical in the statistical sense. In particular, we shall see that the $(\eta, n) = (0.1, -1)$ and $(\eta, n) = (0.1, -1.5)$ simulations are subject to radial orbit instability, as well know from the literature (see, e.g. Cannizzo & Hollister 1992; Hozumi, Fujiwara, & Kan-Ya 1996). All the simulations in this work involved 10 millions particles, except that we performed an additional one with 100 millions particles to examine more closely the case $(\eta, n) = (0.1, -1.5)$. The parameters for the

`Gadget-2` runs, in terms of softening length, force accuracy and time step control, are otherwise the same as in C15.

Table 1 summarizes the parameters used to perform the simulations of this work. In particular, the last two columns give the value of $25\,t_{\rm dyn}$ where

$$t_{\rm dyn} = \sqrt{\frac{3\pi}{\rho}} \tag{8}$$

corresponds to the duration of a full radial orbit in a harmonic potential corresponding to a fixed density ρ. We estimate ρ from the simulations themselves, once the system has reached a quasi-stationary state, either directly at the centre of the system or as the average of the density in a sphere containing 10 percent of the total mass. Our estimates are rather crude but justify the choice of final time equal to 80 and 40 for the warm and cold cases, respectively. Yet, we have to stay aware of the fact that increasing the magnitude of the slope $|n|$ decreases the value of $t_{\rm dyn}$.

3 VISUAL INSPECTION: PHASE-SPACE STRUCTURE AND DENSITY PROFILES

Figures 1 and 2 display, for a typical slice of fixed angular momentum, the phase-space distribution function of the warm and cold `VlaSolve` simulations, respectively. They clearly show already that the system first always experiences an early quiescent phase where $f(r, v_r, j)$ builds a smooth spiral structure in (r, v_r) space, and this is independent of initial conditions. This quiescent phase mixing corresponds exactly to the *violent relaxation* phase first described in Lynden-Bell (1967).

The subsequent evolution of the system, however, depends on initial conditions.

In the warm cases, the spiral structure remains stable and survives during many dynamical times. The only instabilities building up, at least during a long time, are in the outer parts of the system. In this case, the `Gadget-2` simulations agree very well with the `VlasSolve` simulations during all the interval of time considered, $t \in [0, 80]$, even in regions where these instabilities develop, as already noticed by C15 for the $(\eta, n) = (0.5, 0)$ case, showing that these instabilities are of physical nature. A visualisation of a film of the evolution of the system shows that they are induced by a resonance related to a global pulsation of the system. Now we extend this result to $(\eta, n) = (0.5, -0.5)$ and $(0.5, -1.0)$ even though we do not explicitly show it as there is not much more to see than in C15. For $(\eta, n) = (0.5, -1.5)$, the spiral structure seems to be disrupted at some point in both the `VlaSolve` and the `Gadget-2` simulations around $t \sim 30$, and this happens a bit earlier in the `Gadget-2` run. In this case, we suspect that the disagreement between the two simulations is of numerical nature. In particular, discreteness effects might contaminate the measurements in the `Gadget-2` run. However, we cannot either be sure that the `VlaSolve` simulation is correct at late time, because it is also subject to potential aliasing effects due to the relatively small number of slices we chose in angular momentum space. We shall come back to this later. Note that there might be a point where the spiral structure is disrupted in all the cases, similarly as in the cold runs, even for smaller value of $|n|$. We did not push our runs far enough to confirm this state of fact, but as illustrated by the two right columns of Table 1, the $(\eta, n) = (0.5, -1.5)$ case is more evolved dynamically than smaller values of $|n|$, hence prone to experience this instability earlier.

Turning to the cold cases, some radial instabilities develop quickly in phase space and destroy the spiral structure both in the `VlaSolve` and the `Gadget-2` simulations. These instabilities, certainly of the same nature as described first in Hénon (1973) (see also, e.g. Barnes, Hut, & Goodman 1986; Henriksen & Widrow 1997) but for different kinds of initial conditions, take place earlier for larger $|n|$, in agreement with our calculation of dynamical times in the two right columns of Table 1. Careful examination of Fig. 3 helps us to understand more in detail how the instabilities develop according to the numerical technique used. Clearly, one can see that the instability is of numerical nature both in `VlaSolve` and `Gadget-2` runs: in the first case, it is induced by the discrete nature of the grid used to represent the phase-space distribution function, while in the second case, it is due to particle shot noise. These two sources of noise induce some radial anisotropies, hence some small shifts in the orbital times which imprint on the spiral structure perturbations that amplify with time. These instabilities are due to small errors on the force and are of *collective* nature as discussed for instance in detail in C15. They are reduced by respectively augmenting the resolution in the `Vlasolve` code and the number of particles in the `Gadget-2` simulations. For instance, increasing the number of angular momentum slices in the `VlaSolve` simulation reduces the magnitude of the perturbations of the spiral (compare middle insert of first and second line of panels), and similarly when increasing the number N of particles in the `Gadget-2` runs (compare middle insert of third and fourth line of panels).

Note the very striking similarity between the `Gadget-2` (third line of panels) and the shell (last line of panels) simulations with 10^7 particles, with the same pattern of instability, even in the details. This is expected, since the initial positions of the shells is the same in the shell code as in the `Gadget-2` run. However, the only source of error perturbing the calculation of the force in the shell code is a radial component, proportional to $1/\sqrt{N_{\rm interior}}$ where $N_{\rm interior}$ is the number of particles interior to the shell. In the `Gadget-2` simulations, Poisson noise induces, in addition, random angular anisotropies. As argued by Aarseth, Lin, & Papaloizou (1988) these anisotropies are sub-dominant compared to the radial error, at least at sufficiently early times. This is coherent with what we observe in Fig. 3, where the middle inserts of 3rd and 5th lines of panels agree very well with each other. At final time, though (right inserts of 3rd and 5th lines of panels), the `Gadget-2` and shell simulations diverge. In this case, the `Gadget-2` run is subject to radial orbit instability and has indeed developed a strong anisotropy in angular space, hence a significant deviation from spherical symmetry.

Radial orbit instability signature is first found in the velocity anisotropy parameter $\alpha = 2\langle v_r^2\rangle/\langle v_\perp^2\rangle$ where v_r and $v_\perp$ are respectively the radial and transverse velocities, as plotted in left panel of Fig. 4 (see also Hozumi, Fujiwara, & Kan-Ya 1996). Cold initial conditions induce, after collapse, a strong velocity anisotropy, which is known, when exceeding some (still not fully known) threshold, to trigger radial orbit instabilities in presence of small perturbations to spherical

n	η	(N_r, N_v, N_j)	N (`Gadget-2`)	$25\,t_{\rm dyn}$ (centre)	$25\,t_{\rm dyn}$ (10 percent)
0	0.545	(2048, 2048,128)	10^7	108	123
-0.5	0.536	"	"	82	106
-1.0	0.526	"	"	47	77
-1.5	0.515	"	"	13	46
0	0.109	"	"	17	21
-0.5	0.108	"	"	15	24
-1.0	0.106	"	" + shells	9	23
-1.5	0.104	" + (1024,512,512)	" $+10^8$ + shells	4	19

Table 1. Parameters used for the simulations performed in this article. From left to right, it gives the slope n of the initial density profile, the actual value η of the virial ratio after apodization (7), the resolution (N_r, N_v, N_j) of the Vlasov code grid, the number N of particles in the `Gadget-2` simulations, with the mention of when the shell code is used as well. Finally, the two last columns give the approximate value of time after 25 harmonic orbits respectively computed from the density measured at the centre of the simulation and from the average density measured in a sphere containing 10 percent of the total mass of the system, once the system has reached a quasi-stationary regime.

symmetry (see, e.g. Polyachenko & Shukhman 1981; Barnes, Lanzel, & Williams 2009; Maréchal & Perez 2011; Polyachenko & Shukhman 2015, and references therein). The onset of radial orbit instability strongly decreases the velocity anisotropy, as illustrated in left panel of Fig. 4: in the cold cases, the `Gadget-2` simulations suddenly deviate from the `VlaSolve` runs for $n = -1$ and $n = -1.5$. The divergence happens earlier with increasing $|n|$ (compare upper cyan dashed curve to upper red dashed curve) and later with increasing number of particles N (compare upper cyan dashed curve to upper black dashed curve), in agreement with intuition. The n dependence is indeed probably mainly related to different dynamical times as computed in the last two columns of Table 1. For instance, comparing dynamical times obtained from the $(\eta, n) = (0.1, -1.5)$ and the $(\eta, n) = (0.1, -1)$ runs predict a ratio between them ranging from $25/19 = 1.3$ and $10/4 = 2.5$, to be compared with an approximate factor 2 when finding the point $t_{\rm r} \sim 10$ and $t_{\rm r} \sim 20$ marking the beginning of the plateau $\alpha \simeq 2$ on the red and cyan dashed curves, respectively. Note however that radial orbit instability being here triggered by local Poisson fluctuations, it is not obvious to know the error on $t_{\rm r}$ unless performing a number of realizations of `Gadget-2` runs to have a statistically significant sample, which we did not do for the present work, so our estimates of $t_{\rm r}$ should be considered here as very approximate, so far.

Radial orbit instability makes the system non spherical and induces for our systems a prolate shape for the halo, as shown in right panel of Fig. 4. Similarly as in C15, we measure the inertia tensor of the system and diagonalize it to find its eigenvalues $\lambda_1 \geqslant \lambda_2 \geqslant \lambda_3$. From there, we were able to compute the axis ratios of the system with the standard formulae

$$\frac{b}{a} = \sqrt{\frac{\lambda_1 + \lambda_3 - \lambda_2}{\lambda_1 + \lambda_2 - \lambda_3}}, \quad \frac{c}{a} = \sqrt{\frac{\lambda_3 + \lambda_2 - \lambda_1}{\lambda_1 + \lambda_2 - \lambda_3}}, \quad a \geqslant b \geqslant c. \tag{9}$$

The examination of right panel Fig. 4 shows that deviation from spherical symmetry happens simultaneously with velocity anisotropy sudden deviation between `Gadget-2` and `VlaSolve`. However, for the time range probed by our simulations, the system does not really converge to a definite shape, being progressively more and more prolate with time. Clearly, our simulations are not run long enough to have all the details of the history of the halo, which might evolve further to another interesting state. Note also that in the other cold cases, namely $(\eta, n) = (0.1, -0.5)$ and $(0.1, 0)$, radial orbit instability might in fact develop, but at later times than the maximum considered in our analyses, $t_{\rm max} = 40$. The conditions of establishment of radial orbit instability are however not yet fully understood: some theoretical calculation and numerical experiments show that it should take place when $\alpha > \alpha_{\rm critical}$ with $\alpha_{\rm critical}$ ranging between 1 and 2.9 (see, e.g. Polyachenko & Shukhman 2015): the cases $(\eta, n) = (0.1, -0.5)$ and $(0.1, 0)$ are precisely in this range, when examining the plateau at large time of the green curve on left panel of fig. 4, so their fate is undecided. Here, we do not find any signature of radial orbit instability for $t \lesssim 40$.

To complete the analyses of this section, Fig. 5 shows the projected density profile $\rho(r)$ measured at various times in all the simulations. As expected the results obtained with `VlaSolve` agree with a previous analysis performed with a similar code by Hozumi et al. (2000). To confirm the observations above, the density profile provided by the spiral structure built in phase space through standard violent relaxation process (green) is preserved even if the spiral structure is destroyed by instabilities (red dashes), mainly of radial nature. As discussed earlier, the spiral structure seems, in the cold case, unstable with respect to small perturbations induced by the comb nature of the grid used to represent the phase-space in `VlaSolve` and the shot noise of the particles in `Gadget-2` or in the shell code. However, the destruction of this spiral does not affect significantly the projected density profile, as long as radial orbit instability does not take place. If radial orbit instability takes place, $\rho(r)$ is slightly dampened at small radii (see the grey curves on 2 bottom right panels of Fig. 5). Pure radial perturbations due to discreteness do not perturb the density profile as the shell code agrees nearly perfectly with `VlaSolve`.

4 SELF-SIMILARITY IN PHASE-SPACE

Now, we analyse the self-similar properties of our numerical systems, following very closely unpublished work of Alard (2016).

When examining a slice of fixed angular momentum, we notice that the Vlasov equation for a spherical system is

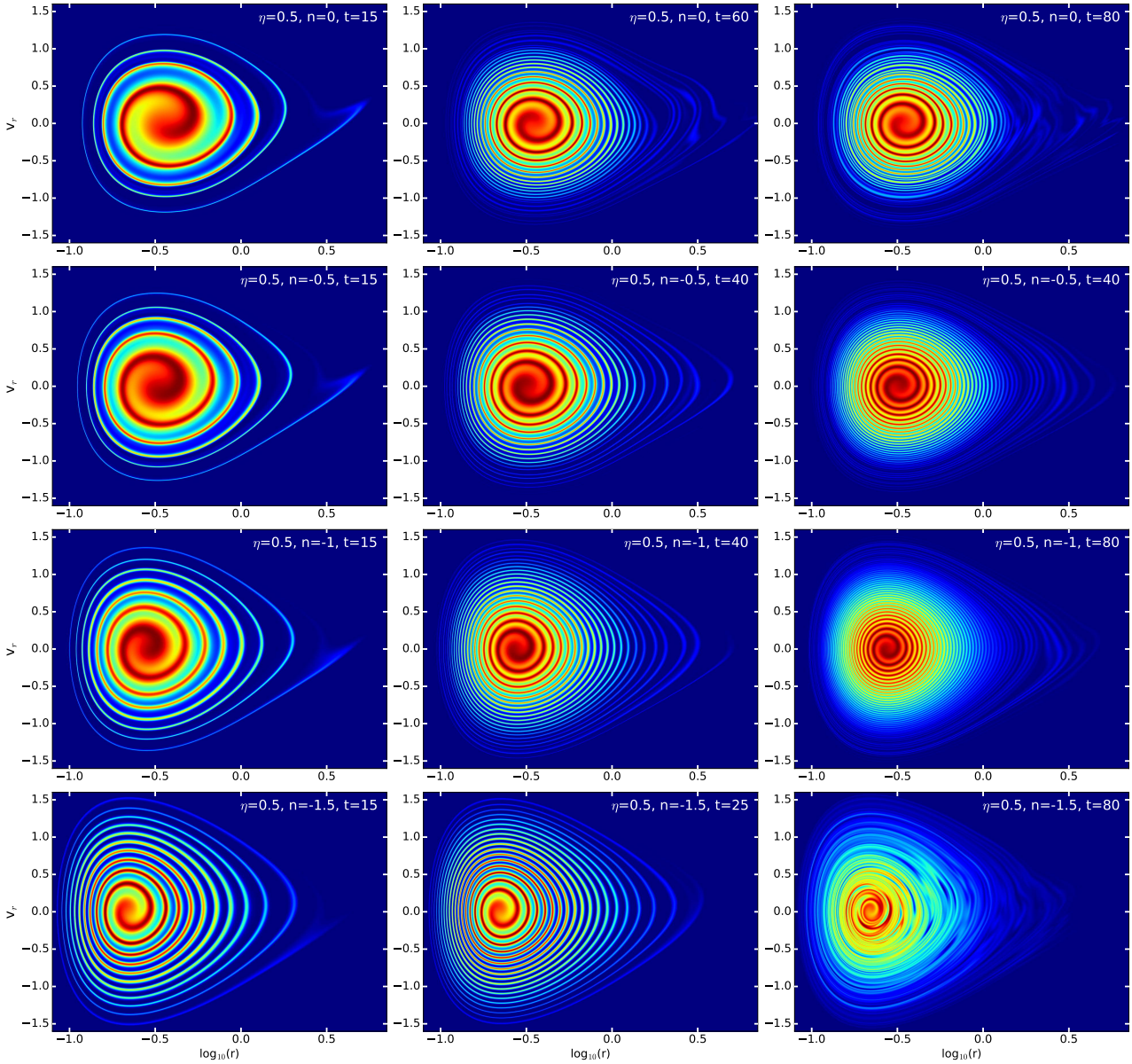

Figure 1. Snapshots of the phase-space density for the simulations with warm initial conditions, $\eta \simeq 0.5$. A typical slice of $f(r, v_r, j)$ with $j = 0.16$ is shown in (r, v_r) space for the `VlaSolve` simulations at an early time $t = 15$ (left panels), at an intermediate time used to perform tests of self-similarity of the phase-space spiral (middle panels) and at the final time (right panels).

exactly analogous to the one-dimensional case:

$$\frac{\partial f}{\partial t} + v_r \frac{\partial f}{\partial r} - \frac{\partial \tilde{\phi}}{\partial r} \frac{\partial f}{\partial v_r} = 0, \tag{10}$$

except that the force derives from the following scalar field

$$\tilde{\phi}(r) = \frac{j^2}{2r^2} + \phi(r), \tag{11}$$

where $\phi(r)$ is the gravitational potential. A13 derived detailed self-similar solutions in the 1D case that we extend below in the regimes where the inertial force dominates $\tilde{\phi}(r) \simeq j^2/(2r^2)$ and in the regime where gravitational potential dominates and is a power-law, $\phi(r) \propto r^{\beta+2}$. The transition between these two regimes is rather sharp, as illustrated by Fig. 6.

Assuming that the conserved angular momentum j is a dummy variable, the self-similar solution for the phase-space distribution function can be expressed as follows:

$$f(r, v_r, j) = t^{\alpha_0} F_j \left(\frac{r}{t^{\alpha_1}}, \frac{v_r}{t^{\alpha_2}} \right). \tag{12}$$

Setting

$$\tilde{r} = \frac{r}{t^{\alpha_1}}, \quad \tilde{v} = \frac{v_r}{t^{\alpha_2}}, \tag{13}$$

We can express both the gravitational and the inertial force

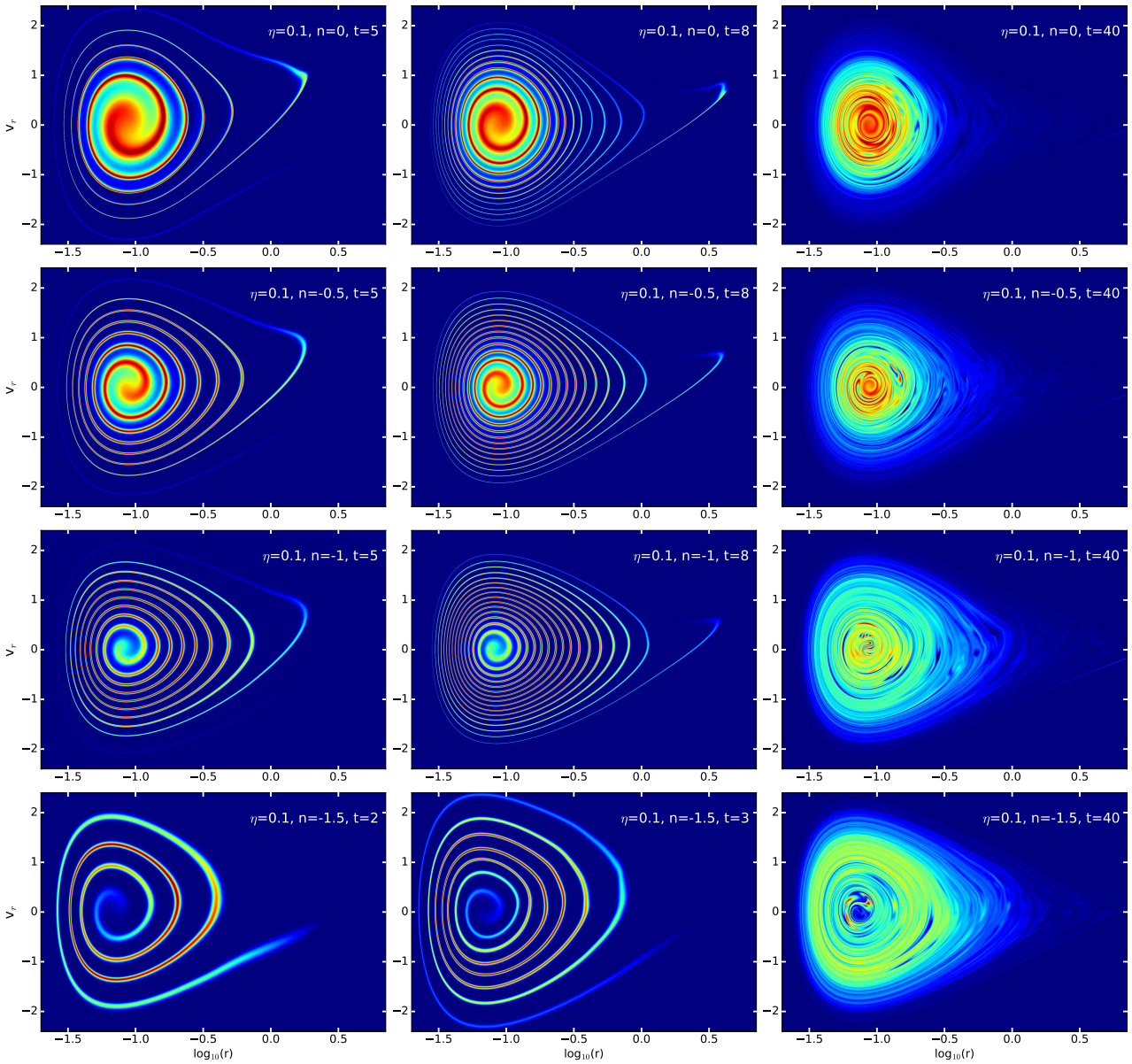

Figure 2. Same as in Fig. 1 but for the simulations with cold initial conditions, $\eta \simeq 0.1$ and for a slice with $j = 0.06$.

as functions of these new variables

$$-\frac{\partial\phi}{\partial r} = t^{\alpha}U(\tilde{r}), \quad (14)$$

$$\alpha = \alpha_0 + \alpha_2 - \alpha_1, \quad (15)$$

$$U(\tilde{r}) = -\frac{G}{\tilde{r}^2}\int_{\tilde{r}'<\tilde{r}} 8\pi^2 F_j(\tilde{r}',\tilde{v})\mathrm{d}\tilde{r}'\mathrm{d}\tilde{v}j\mathrm{d}j, \quad (16)$$

$$= -k(\beta+2)\tilde{r}^{\beta+1}, \quad (17)$$

where we assumed in the last equation that $U = -\mathrm{d}\tilde{\phi}/\mathrm{d}\tilde{r}$ and

$$\tilde{\phi}(\tilde{r}) \equiv k\,\tilde{r}^{\beta+2}. \quad (18)$$

Similarly the inertial force can be written

$$\frac{j^2}{r^3} = t^{\alpha}U(\tilde{r}), \quad (19)$$

$$\alpha = -3\alpha_1, \quad (20)$$

$$U(\tilde{r}) = -k(\beta+2)\tilde{r}^{\beta+1}, \quad (21)$$

$$\beta = -4, \quad (22)$$

$$k = \frac{j^2}{2}. \quad (23)$$

By injecting these various expressions in the Vlasov expression one obtains

$$\alpha_0 F_j + \frac{\partial F_j}{\partial\tilde{r}}\left[-\alpha_1\,\tilde{r} + \tilde{v}\,t^{\alpha_2-\alpha_1+1}\right] + \frac{\partial F_j}{\partial\tilde{v}}\left[-\alpha_2\,\tilde{v} - k\,(\beta+2)\,\tilde{r}^{\beta+1}t^{\alpha-\alpha_2+1}\right] = 0. \quad (24)$$

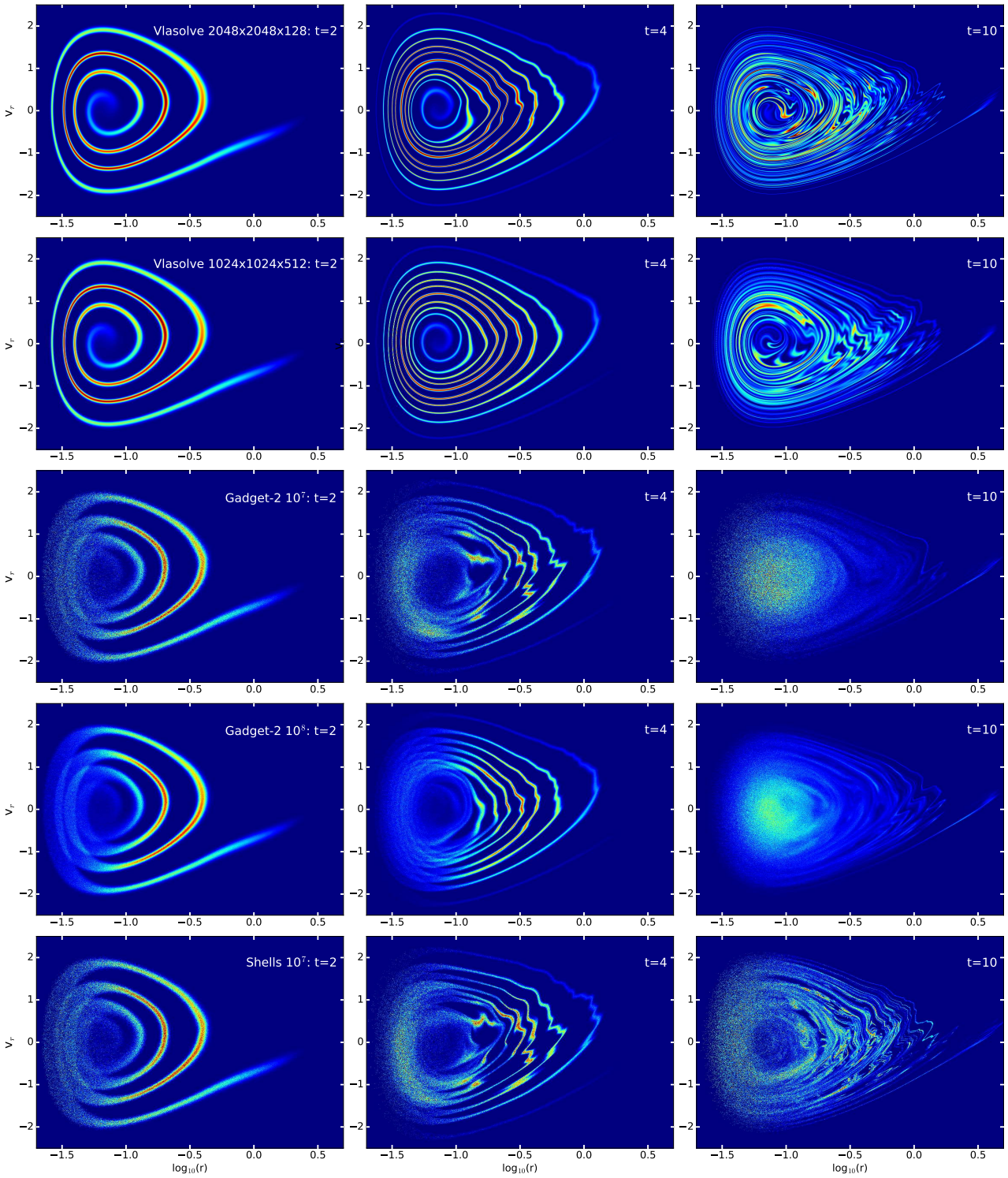

Figure 3. Closer examination of the onset of instabilities in phase space for the $(\eta, n) = (0.1, -1.5)$ simulations. For the same angular momentum slice, $j = 0.06$, as in lower panels of Fig. 2, the phase space density is represented in (r, v_r) space. The two first lines of panels correspond to two `VlaSolve` simulations with respective resolutions $(N_r, N_v, N_j) = (2048, 2048, 128)$ and $(1024, 512, 512)$. The next two lines of panels correspond to two `Gadget-2` simulations with respective numbers of particles $N = 10^7$ and $N = 10^8$ and the last line of panels gives, for $N = 10^7$, the result obtained for the shell code. One can notice that the phase-space sheet is more fuzzy in the N-body simulations than in the Vlasov code at low radius, this is because what is actually plotted is the distribution of particles (or shells) in a relatively large interval of angular momentum $j \in [0.056, 0.077]$ to have sufficient number of particles to trace the phase-space distribution function, while for the Vlasov simulation, we just selected the slice corresponding to the value of j of interest.

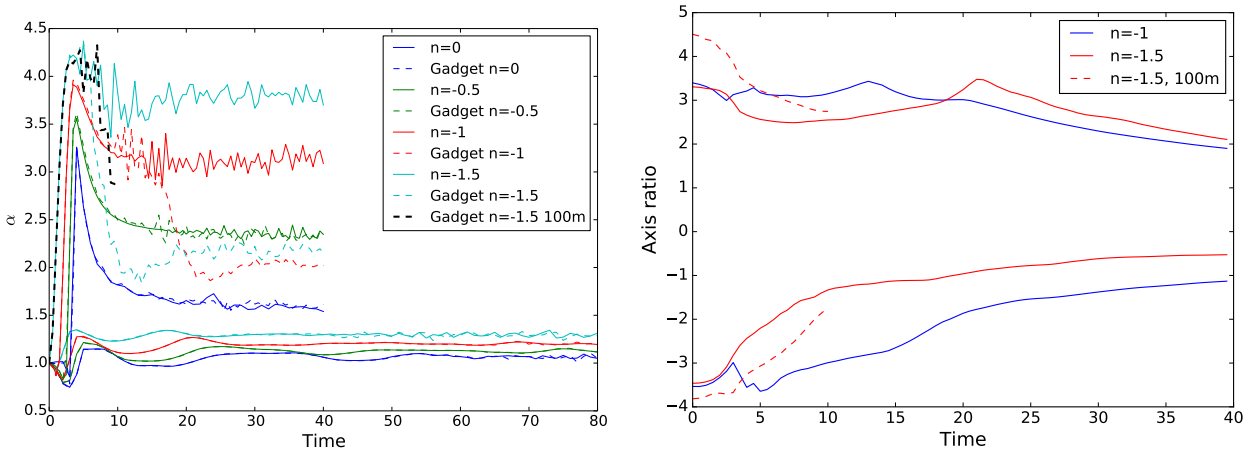

Figure 4. Velocity anisotropy and deviation from sphericity. Left panel: velocity anisotropy parameter $\alpha = 2\langle v_r^2\rangle/\langle v_\perp^2\rangle$ as a function of time for the `VlaSolve` (solid lines) and `Gadget-2` simulations we performed (dashed curves). Right panel: evolution of the departure from spherical symmetry for the two simulations experiencing radial orbit instability, namely $(\eta, n) = (0.1, -1.0)$ (blue curves) and $(\eta, n) = (0.1, -1.5)$ (red curves, solid for the 10 millions particles simulation and dashed for the 100 millions particles simulation, respectively). The quantity $\mathrm{sgn}(1 - \mathrm{r_{axis}}) \log_{10} |1 - \mathrm{r_{axis}}|$ is plotted as a function of time, where $r_{\rm axis} = b/c$ (upper curves) or b/a (lower curves) and $a \leqslant b \leqslant c$ are the principal axe lengths of the `Gadget-2` particle distribution derived from the inertia tensor.

Eliminating time dependence in this equation imposes

$$\alpha_1 = \alpha_2 + 1, \tag{25}$$

$$\alpha = \alpha_2 - 1. \tag{26}$$

Imposing furthermore stationarity of the force $t^\alpha U(r/t^{\alpha_1})$ assuming the power-law (17) for U imposes

$$\alpha - (\beta + 1)\alpha_1 = 0. \tag{27}$$

Hence the only viable solution is

$$\alpha_2 = -\frac{\beta + 2}{\beta}, \tag{28}$$

$$\alpha_1 = -\frac{2}{\beta}, \tag{29}$$

$$\alpha = -\frac{2\beta + 2}{\beta}, \tag{30}$$

which is of course consistent with equation (20) if the inertial force dominates and leaves α_0 a free parameter, while, if the gravitational force dominates, this imposes a value for α_0 to be fixed to $\alpha_0 = -(\beta + 2)/\beta$. Note that, in general, total mass is not conserved. Indeed, enforcing total mass conservation (or mass conservation per angular momentum slice, as well), imposes $\alpha_0 + \alpha_1 + \alpha_2 = 0$, a condition which is fulfilled only for $\beta = -3/2$ and in this case $\alpha_0 = 1/3$. This is not a problem because self-similarity is expected to take place only in a finite dynamical range.

Setting, to follow as closely as possible the notations of A13,

$$\mathcal{G} \equiv \ln F_j, \tag{31}$$

$$\eta \equiv \frac{\beta}{2} + 1, \tag{32}$$

$$u \equiv \tilde{r}^\eta, \tag{33}$$

we obtain the following equation:

$$-\alpha_0 + (1 + \alpha_2)\,\eta\,\frac{\partial \mathcal{G}}{\partial u} u + \alpha_2 \frac{\partial \mathcal{G}}{\partial \tilde{v}} \tilde{v} - \eta \left[\frac{\partial \mathcal{G}}{\partial u}\tilde{v} - 2\,k\,u \frac{\partial G}{\partial \tilde{v}}\right] u^{\beta/(\beta+2)} = 0, \tag{34}$$

which is exactly the same equation as equation 11 of A13, except that the first term $\alpha_2 + 2$ is replaced here with $-\alpha_0$. Hence the solution of this equation is very similar to the expressions given in A13. The main difference here is that the values of β we consider are outside the domain of validity of the calculations of A13, which implies that the isocontours of the solutions are closer to hyperbolic curves than to a spiral. However, here, we have to take into account the fact that we have two distinct supposed self-similar regimes, one dominated by inertial force, say for $r \lesssim r_{\rm crit}(j)$, and the other dominated by gravitational force, say for $r \gtrsim r_{\rm crit}(j)$. Hence the actual solution is the connection between too partial solutions which follow self-similar properties.

Rescaling variable $\tilde{r}$ so that $k = 1/2$ in equation (18), and introducing, exactly as in A13, the new variables

$$R = \sqrt{u^2 + \tilde{v}^2}, \tag{35}$$

$$\cos\Psi = \frac{u}{R}, \tag{36}$$

we obtain nearly exactly equation 12 of A13, but the parameters of this equation change according to whether the value of $R\cos\Psi$ is above or below a threshold fixed by $r_{\rm crit}$. With $H(R, \Psi) \equiv G(u, \tilde{v})$ we write, following exactly the footsteps of A13, the general solution for H when the power-law force is stationary

$$H(R,\Psi) = \frac{\alpha_0}{\alpha_2}\ln R + Q\left(R^{-1/\alpha_2} + \frac{1+\alpha_2}{\alpha_2}\int (\cos\Psi)^{1/\alpha_2} \mathrm{d}\Psi\right), \tag{37}$$

with $\Psi \in]-\pi/2, \pi/2[$ and where Q is some function. At this point, introducing the same concept of spiral as in A13 is

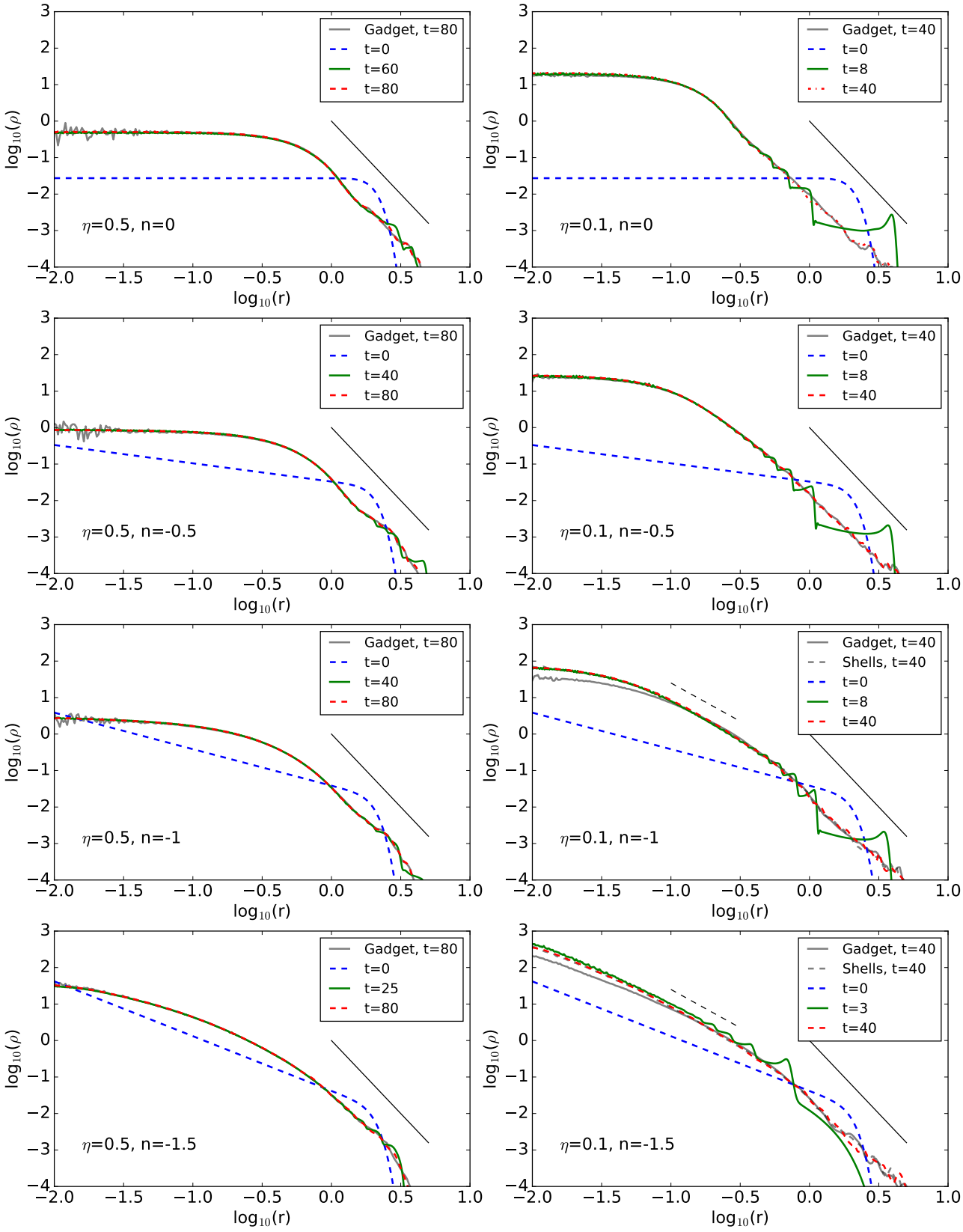

Figure 5. Radial density profile measured at various times in the `VlasSolve` simulations, namely initial conditions (blue dashes), intermediate time used to perform tests of self-similarity of the phase-space spiral (green) and final time (red dashes). For the final time, the results are also compared to a `Gadget-2` run (thick grey), as well as the output of the shell code (thick grey dashes) for $(\eta, n) = (0.1, -1)$ and $(0.1, -1.5)$. In addition, the logarithmic slopes -4 and -2.1 (as measured in Hozumi et al. 2000) are shown respectively as a thin solid and a thin dashed line.

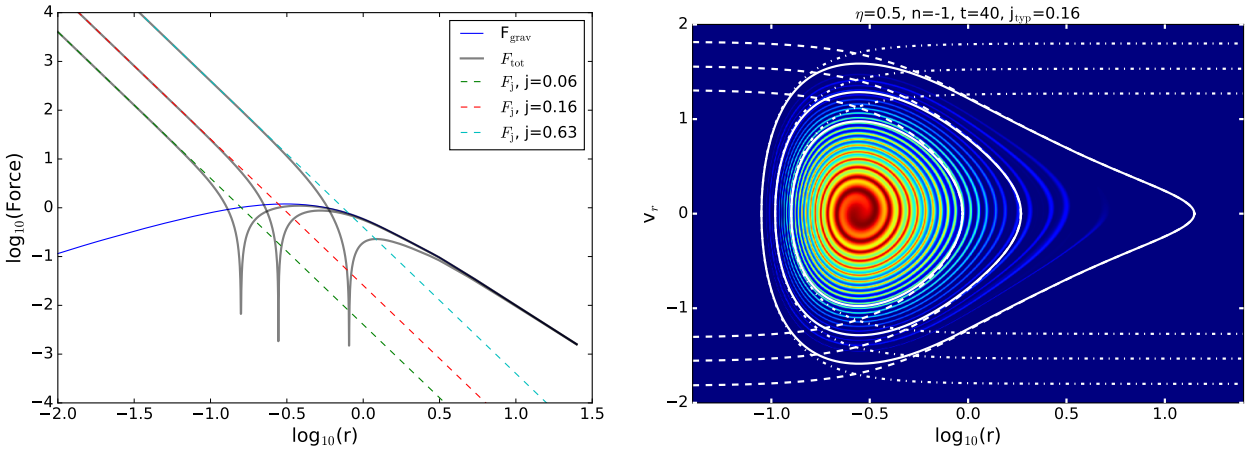

Figure 6. The small and large radii regimes in the $(\eta, n) = (0.5, -1)$ `VlaSolve` run at $t = 40$. Left panel plots separately the magnitude of inertial force j^2/r^3 and of the gravitational force as functions of radius as well as the magnitude of the sum of both forces. Right panel show isocontours of the specific energy (white curves) superposed on the phase-space distribution function for $j = 0.16$. In addition, the white dashes and dot-dashes assume respectively that only the gravitational and the inertial force contributes.

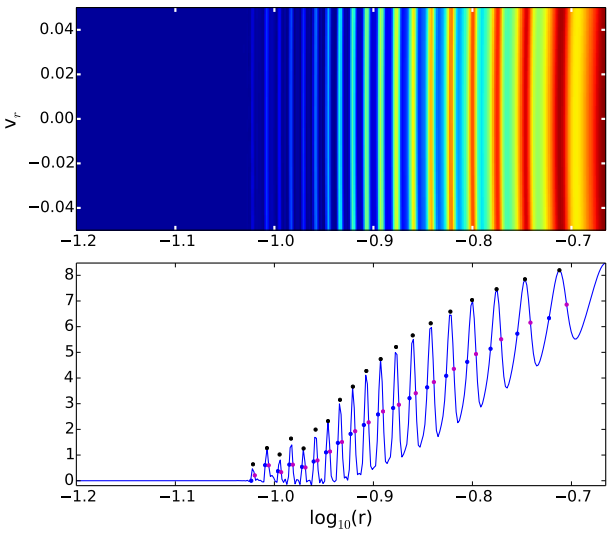

Figure 7. Illustration of the method to determine the position of the folds and corresponding interfold distance law at small radius in a phase-space slice. On top panel, a zoom is performed around the axis $v_r = 0$ in the region dominated by inertial force for the $(\eta, n) = (0.5, -1.0)$ simulation at $t = 40$. The corresponding phase-space distribution function $f(r, v_r = 0, j = 0.16)$ is plotted on lower panel. The black dots give the positions of local maxima estimated with our local quadratic fit, while the blue and red dot provide upper and lower bounds to compute the error bars shown on Fig. 8.

not simple, because the fact that $u > 0$ does not allow Ψ to make a full excursion on the circle. Furthermore, the values of logarithmic density profile slope β we have to consider range in the interval $-4 \lesssim \beta < -2$, which implies, from equation (28), $-1/2 \lesssim \alpha_2 < 0$, hence some divergence of the integral

$$I \equiv \frac{1+\alpha_2}{\alpha_2} \int (\cos\Psi)^{1/\alpha_2} \mathrm{d}\Psi, \tag{38}$$

when $|\Psi|$ approaches $\pi/2$. This is however not a real problem, because the point here is to connect two self-similar solutions. Here, we are unable to demonstrate the existence of the spiral structure in phase-space, we have to postulate it. We therefore define a new angular variable θ and

$$I(\theta) \equiv \int g(\theta')\mathrm{d}\theta', \tag{39}$$

where $g(\theta)$ is a function of period 2π verifying

$$g(\theta) \simeq g_-(\theta) \equiv \frac{1+\alpha_2^-}{\alpha_2^-}[\cos(\Psi^- = \theta - 2k\pi)]^{1/\alpha_2^-}, \quad \theta - 2k\pi \simeq 0, \tag{40}$$

$$g(\theta) \simeq g_+(\theta) \equiv \frac{1+\alpha_2^+}{\alpha_2^+}[-\cos(\Psi^+ = \theta - 2k\pi)]^{1/\alpha_2^+}, \quad \theta - 2k\pi \simeq \pi, \tag{41}$$

and $-$ and $+$ correspond respectively to the regimes dominated by the inertial and the gravitational force. Function $g(\theta)$ makes a smooth transition between g_- and g_+. The only, trivial but important fact we have to know, is that $I(\theta)$ defined this way is roughly proportional to θ which allows us now to define explicitly the concept of a spiral across both self-similar domains. The interesting bit is that the subsequent calculations of A13 are not changed at all when taking this new definition of I and his equation 19 still stands in each self-similar domain, with $I_1 = \int_0^{2\pi} g(\theta')\mathrm{d}\theta'$ now a unknown constant instead of a well defined integral as in A13.

Hence, we have, in the situation where there are many folds, the following expected relationship for the interfold distance in each self-similar region

$$\mathrm{d}R \propto R^{1+1/\alpha_2}. \tag{42}$$

In particular, coming back to standard variables (r, v_r), the interfold distances along the axis $v_r = 0$ reads

$$\mathrm{d}r \propto r^{1-\beta/2}. \tag{43}$$

To test this property directly, we analyse, at a time where the spiral structure is still well defined, function $f(r, v_r = 0, j)$ for a fixed value of angular momentum, as illustrated

by Fig. 7. We determine the positions of the folds using local parabolic fits. For each fold i, we determine two semi-heights radial positions $\log(r_{\mathrm{l},i})$ and $\log(r_{\mathrm{r},i})$ (the computational grid being logarithmic in radius), on the left and on the right of the peak (respectively), and define the error on the position of the peak as $\delta \log(r_i) = \log(r_{\mathrm{r},i}) - \log(r_{\mathrm{l},i})$.

Fig. 8 summarizes the results of our measurements in the `VlaSolve` simulations. At "small" radius, the system is dominated by the inertial force, $\beta = -4$, hence $\mathrm{d}r \propto r^3$. This prediction is compared to measurements in the simulations in the first and third columns of Fig. 8, which correspond respectively to the simulations with warm and cold initial conditions. At "large" radius, where the system is dominated by gravity, the force is only approximately a power-law but an average slope can nevertheless be inferred in some interval of scales E_{grav}, corresponding to the regime where the gravitational force remains at least ten times larger than the inertial force and for r smaller than the turnaround radius. On second and fourth column of panels of Fig. 8, the slope of the red line is given by the corresponding value of $1 - \beta/2$. There are also two dashed cyan and green lines corresponding to the minimum and maximum value of β found in E_{grav}, which gives an idea of deviation from a pure power-law. Globally, the simulations agree rather well with self-similar predictions, except maybe at very small radius on first and third columns of panels and in top insert of the second column of panels. Note however that measurement of interfold distance for small values of r might be partly spurious, because we are in a regime where the phase-space distribution function is small and can be affected by aliasing. Also, notice that the spiral structure survives only shortly for $(\eta, n) = (0.1, -1.5)$ which leaves us with only a small number of folds to deal with. Yet, the agreement with self-similarity remains good when taking into account the limitations found in all cases at very small r, already after only a few dynamical times.

Another interesting property than can be derived directly from equation (37) is the local shape of the spiral near the axis $v_r = 0$, hence $\Psi \simeq 0$, and for small r, hence small R. Following the unnumbered equation after equation 16 of A13 and taking into account the fact that $\alpha_2 < 0$, we expect an isocontour of the function $H(R, \Psi)$ to have the following shape in the regime $R \ll 1$, $\Psi \simeq 0$,

$$R \propto \Psi^{-\alpha_2} \propto \Psi^{(\beta+2)/\beta}. \tag{44}$$

Note thus that because of the form of the interfold law (42), the spiral actually coincides locally with a curve defined by $R \propto \theta^{-\alpha_2}$ with θ playing the same role as Ψ, but no longer restricted to $]-\pi/2, \pi/2[$, instead, this interval and its multiples $]-\pi/2+2k\pi, \pi/2+2k\pi[$. Left panel of figure 9 nicely illustrates how this prediction matches well the local spiral shape of the simulated phase-space distribution function, including its local curvature, in the regime dominated by the inertial force ($\beta = -4$) for $(\eta, n) = (0.5, -1.0)$.

In middle panel of this figure, we also check, in the regime dominated by inertial force, for self-similarity in time of the spiral shape, namely that if one considers the system at two different times, t_1 and t_2, the state at $t = t_2$ should superpose to the state at $t = t_1$ rescaled as follows

$$v_r(t_1) \quad \rightarrow \quad v_r(t_1) \left(\frac{t_2}{t_1}\right)^{\alpha_2}, \tag{45}$$

$$r(t_1) \quad \rightarrow \quad r(t_1) \left(\frac{t_2}{t_1}\right)^{\alpha_1}. \tag{46}$$

Of course, since we have two distinct self-similar regimes, this property works well only in the neighbourhood of $v_r \simeq 0$ and for values of r where the gravitational force is subdominant compared to the inertial force.

Finally, right panel of Fig. 9 shows that if gravitational potential is known, the spiral shape of the phase-space distribution function can be fully reconstructed accurately just by knowing its intersection with the $v_r = 0$ axis in the regime dominated by angular momentum (or reversely, in the regime dominated by gravitational force) by simple linear interpolation of the specific energy E along the spiral during an orbit in the following Angle coordinate $\mathcal{A}$,

$$\mathcal{A}(s, E) \quad \equiv \quad 2\pi \frac{\tau(s, E)}{T(E)}, \tag{47}$$

$$\tau(s, E) \quad = \quad \int_0^s \frac{\mathrm{d}r(s')}{v_r(s')}, \tag{48}$$

$$T(E) \quad = \quad \oint \frac{\mathrm{d}r(s')}{v_r(s')}, \tag{49}$$

where s is a curvilinear coordinate. This technique was actually used to draw the spiral of middle panel. Of course, this result is kind of trivial from the dynamical point of view. However, it suggests that passing to Action-Angle space or energy-Angle as performed here may represent the right way to smoothly connect both self-similar regimes and therefore to have a full analytic description of the fine grained structure of the phase-space distribution function. To do this, one needs to relate locally the angular variable Ψ intervening in the self-similar solutions to the Angle given by equation (49), but this is left for future work.

5 CONCLUSION

In this article, we have analysed in detail the phase-space structure of various systems with spherical initial conditions, consisting in a power-law density profile with a Gaussian velocity dispersion. Two cases were considered, the "warm" set-up with virial ratio $\eta \simeq 0.5$ and the "cold" one with $\eta \simeq 0.1$. The choice of such initial conditions is not really new but the numerical set-up is different from what can be found in the literature. Firstly, we compare three kind of codes, a Vlasov code, a treecode and a shell code. Secondly we perform this comparison with unprecedented numerical resolution, namely $(N_r, N_v, N_j) = (2048, 2048, 128)$ for the Vlasov code and 10 millions particles for the N-body simulations, up to 100 millions for one `Gadget-2` run. This allowed us to study all the fine details of the phase-space distribution function.

For all the simulations we did, we find that the system always builds up a smooth spiral structure in phase-space and converges quickly towards a quasi-stationary regime while the spiral winds up. Although this is not really new, the existence of this quiescent regime for a large range of initial conditions was never really proved numerically in a

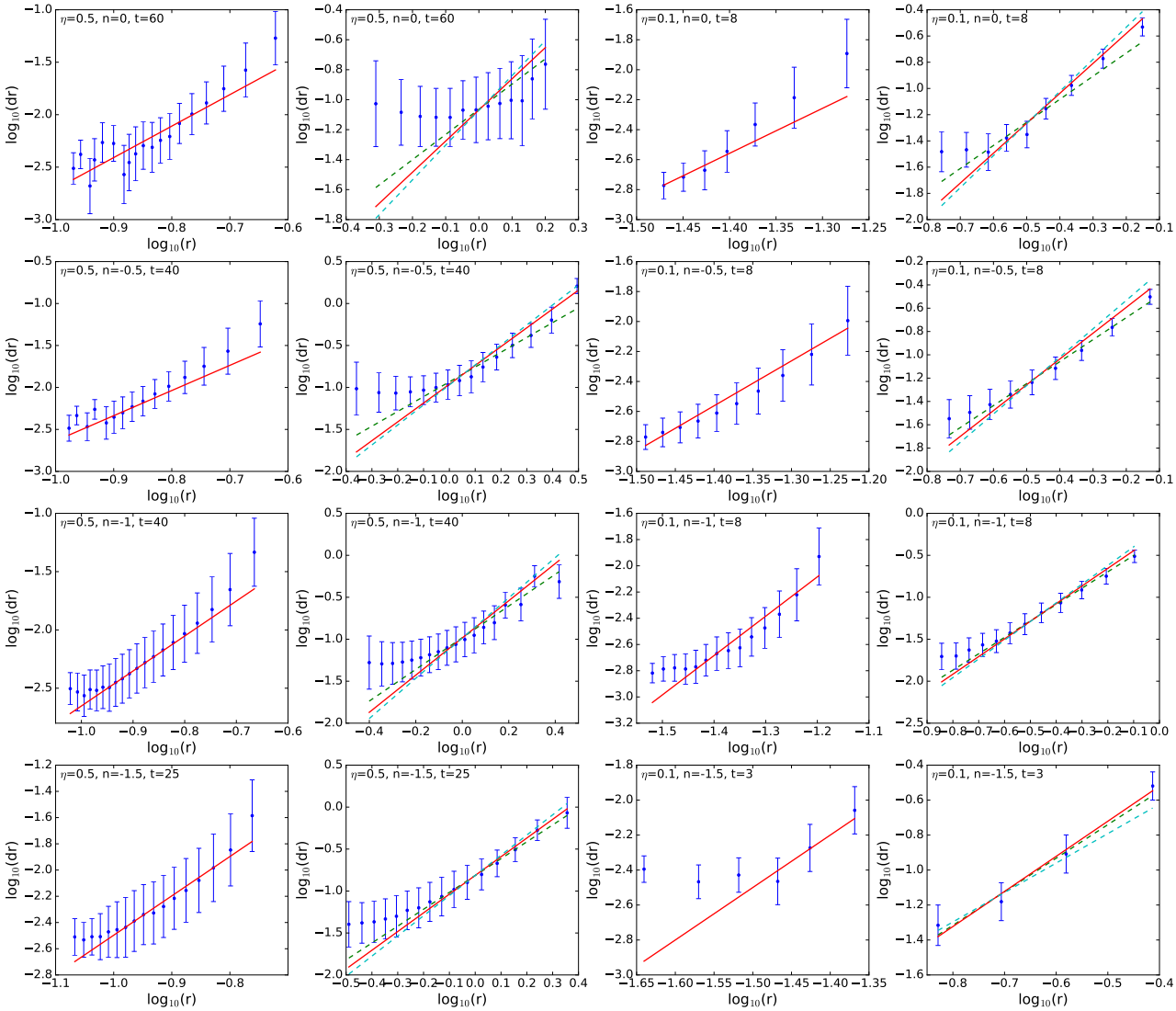

Figure 8. Interfold distance at null radial velocity versus self-similar predictions for a fixed value of angular momentum. The distance dr between local maxima of the function $f(r, v_r = 0, j)$ is plotted as a function of r for the `VlaSolve` runs with various initial conditions. The time considered correspond to middle column of panels in Figs. 1 and 2. The two lefts columns of panels correspond to the warm case, $\eta = 0.5$ with $j = 0.16$, and the two right ones to the cold case, $\eta = 0.1$ with $j = 0.06$. Then, odd column number (1 and 3) and even column number (2 and 4) correspond to the regime where inertial/gravitational force dominates, respectively. On each panel a red line indicates the logarithmic slope predicted by self-similarity. When the gravitational force dominates, two additional dashed curves provide a bracket of the estimated slope taking into account deviations from self-similarity, i.e. variations of the effective logarithmic slope of the gravitational force.

systematic way. We studied in detail the fine structure of this spiral and found that it agrees well with predictions of self-similarity in regimes where inertial and gravitational forces dominate, respectively. A full analytical formalism connecting both regimes in a smooth way to have a global description of the dynamics involved in the evolution of the spiral remains to be developed, but we have hints here that combining self-similar solutions with an Action-Angle approach might be promising.

At some point, the spiral structure can be perturbed or even erased. Indeed, some radial instabilities take place in all the simulated systems, at least in the outskirts of the halo. In the cold simulations, these radial instabilities completely destroy the spiral shape. The nature of the radial instabilities is twofold. The unstable nature of the outskirts of the system that can be observed in the warm case for $n \geqslant -1$ is physical and is related to oscillations of the gravitational potential (the system "pulses" in phase-space). On the other hand, the radial instabilities destroying the spiral structure in the cold case are definitely of numerical nature and are due to collective, systematic errors on the force. For the N-body simulations, this is related to Poisson noise in $1/\sqrt{N}$, but analogous discreteness effects due to the grid used to represent the phase-space distribution function in the Vlasov code have similar consequences. The better the resolution or the larger the number of particles, the longer it

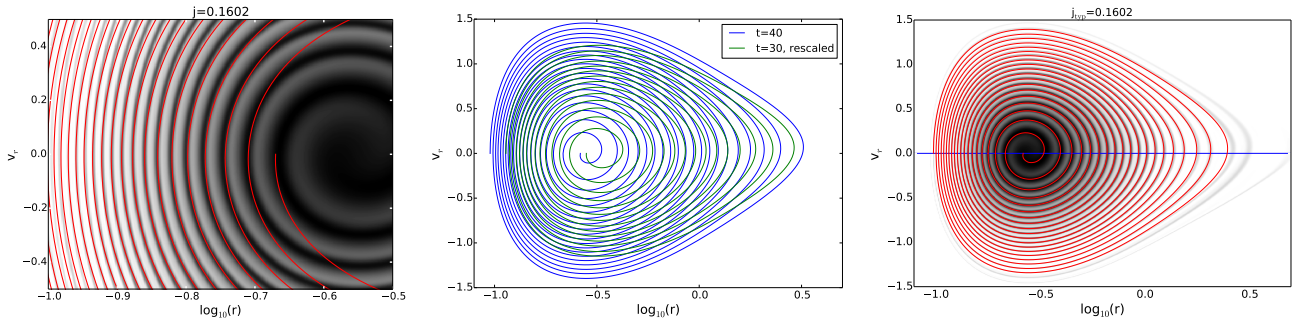

Figure 9. Spiral shape versus self-similar predictions for the `VlaSolve` run with $(\eta, n) = (0.5, -1.0)$. Left panel: comparison, at $t = 40$, of the local shape of the spiral structure in the region dominated by inertial force to the curve given by equation (44) (red curve). Middle panel: test for self-similarity in time. The green spiral shape obtained at $t = 30$, is rescaled according to equations (45) and (46) to be compared to the blue one, in the regime dominated by inertial force. Right panel: using only the determination of the position of the folds in the region dominated by inertial force, it is possible to draw the full shape of the spiral if the gravitational potential is known, by interpolating the specific energy in Angle coordinate defined by equations (47), (48) and (49).

takes for the spiral structure to be destroyed by numerical artefacts. We can therefore easily postulate that, at least in the cold case, the spiral represents an unstable quasi-stationary state of the system.[1] However, the destruction of the spiral structure by radial instabilities does not change the properties of the system at the coarse level. In particular the projected density, $\rho(r)$, remains the same as that obtained from the spiral structure before its destruction. It means that the quasi-stationary state built with the spiral is stable at the coarse level, except when radial orbit instability takes place, but even in this case, the spherically averaged density profile does not change dramatically. For $n \lesssim -1$ and in the cold case, $\eta = 0.1$, the systems indeed experiences radial orbit instability, in agreement with previous results of the literature and with theoretical predictions, hence deviations from spherical symmetry in the `Gadget-2` runs.

Putting aside radial orbit instability, we see thus that if one were able to have an analytic theory to describe the spiral structure generated during the quiescent stage of the evolution of our systems, it would be possible to predict the quasi-stationary state towards the system converges and that persists at the coarse level despite radial instabilities. One way to explore this consists in trying to connect self-similar solutions, as discussed above. Another commonly used way is based on entropy maximisation. However, the results of our analyses suggest that this later is prone to fail in finding the quasi-equilibrium solution, except by coincidence. Indeed, the spiral structure provides the quasi-stationary state of the system at the coarse level *before* being destroyed. Hence, we have a system which builds its quasi-stationary state from a non random process, which seems incompatible with a maximum likelihood approach such as entropy maximisation. The only way, in this case, for maximum entropy to work would be to show that the mapping from micro states to macro states of an evolving spiral looks sufficiently random.

[1] Note that because we run our simulations only during a finite amount of time and with finite resolution, we are unable to show that the spiral structure would survive forever in the continuous limit: it might at some point be destroyed by actual physical resonances analogous to the oscillations inducing the instabilities in the outskirts of the halo observed in the warm case for $n \geqslant -1$.

ACKNOWLEDGEMENTS

We thank C. Alard for providing us the main insights about the analyses performed in § 4, T. Sousbie and S. Hozumi for stimulating discussions. This work was supported in part by ANR grant ANR-13-MONU-0003. We also acknowledge the support of YITP in organising the workshop "Vlasov-Poisson: towards numerical methods without particles" in Kyoto, funded by grant YITP-T-15-02, ANR grant ANR-13-MONU-0003 and by Institut Lagrange de Paris (ANR-10-LABX-63 and ANR-11-IDEX-0004-02).

REFERENCES

Aarseth S. J., Lin D. N. C., Papaloizou J. C. B., 1988, ApJ, 324, 288
Alard C., 2013, MNRAS, 428, 340 (A13)
Alard C., 2016, private communication
Alard C., Colombi S., 2005, MNRAS, 359, 123
Arad I., Johansson P. H., 2005, MNRAS, 362, 252
Barnes J., Hut P., Goodman J., 1986, ApJ, 300, 112
Barnes E. I., Lanzel P. A., Williams L. L. R., 2009, ApJ, 704, 372
Bernardeau F., Colombi S., Gaztañaga E., Scoccimarro R., 2002, PhR, 367, 1
Bertschinger E., 1985, ApJS, 58, 39
Bertschinger E., 1998, ARA&A, 36, 599
Besse N., Sonnendrücker E., 2003, JCoPh, 191, 341
Binney J., 2004, MNRAS, 350, 939
Boily C. M., Athanassoula E., Kroupa P., 2002, MNRAS, 332, 971
Cannizzo J. K., Hollister T. C., 1992, ApJ, 400, 58
Carron J., Szapudi I., 2013, MNRAS, 432, 3161
Cheng C. Z., Knorr G., 1976, Journal of Computational Physics, 22, 330
Colombi S., 2001, NewAR, 45, 373
Colombi S., Sousbie T., Peirani S., Plum G., Suto Y., 2015, MNRAS, 450, 3724 (C15)

Colombi S., Touma J., 2008, Communications in Nonlinear Science and Numerical Simulations, 13, 46
Dehnen W., Read J. I., 2011, EPJP, 126, 55
Dolag K., Borgani S., Schindler S., Diaferio A., Bykov A. M., 2008, SSRv, 134, 229
Filbet F., Sonnendrücker E., Bertrand P., 2001, JCoPh, 172, 166
Fillmore J. A., Goldreich P., 1984, ApJ, 281, 1
Fujiwara T., 1983, PASJ, 35, 547
Gott J. R., III, Thuan T. X., 1976, ApJ, 204, 649
Hénon M., 1964, Annales d'Astrophysique, 27, 83
Hénon M., 1973, A&A, 24, 229
Henriksen R. N., Widrow L. M., 1995, MNRAS, 276, 679
Henriksen R. N., Widrow L. M., 1997, Physical Review Letters, 78, 3426
Hjorth J., Williams L. L. R., 2010, ApJ, 722, 851
Hockney R. W., Eastwood J. W., 1988, Bristol: Hilger, Computer Simulation Using Particles
Hozumi S., Fujiwara T., Kan-Ya Y., 1996, PASJ, 48, 503
Hozumi S., Burkert A., Fujiwara T., 2000, MNRAS, 311, 377
Joyce M., Marcos B., Sylos Labini F., 2009, MNRAS, 397, 775
Joyce M., Worrakitpoonpon T., 2011, PhRvE, 84, 011139
Kandrup H. E., Smith H., Jr., 1991, ApJ, 374, 255
Lynden-Bell D., 1967, MNRAS, 136, 101
Maréchal L., Perez J., 2011, TTSP, 40, 425
Melott A. L., 2007, arXiv, arXiv:0709.0745
Melott A. L., Shandarin S. F., Splinter R. J., Suto Y., 1997, ApJ, 479, L79
Mohayaee R., Shandarin S. F., 2006, MNRAS, 366, 1217
Navarro J. F., Frenk C. S., White S. D. M., 1996, ApJ, 462, 563
Navarro J. F., Frenk C. S., White S. D. M., 1997, ApJ, 490, 493
Polyachenko V. L., Shukhman I. G., 1981, SvA, 25, 533
Polyachenko E. V., Shukhman I. G., 2015, MNRAS, 451, 601
Pontzen A., Governato F., 2013, MNRAS, 430, 121
Sikivie P., Tkachev I. I., Wang Y., 1997, Phys. Rev. D, 56, 1863
Sousbie T., Colombi S., 2016, JCoPh, 321, 644
Springel V., 2005, MNRAS, 364, 1105
Yamaguchi Y. Y., 2008, PhRvE, 78, 041114
Yoshikawa K., Yoshida N., Umemura M., 2013, ApJ, 762, 116